Supplementary Information for

Kinematic self replication in reconfigurable organisms

Sam Kriegman*, Douglas Blackiston*, Michael Levin, and Josh Bongard

Table of Contents:

Supplemental Movie S1

A swarm of frog-cell parents push frog cells into piles that mature into self-moving “children”. An AI method optimizes the original spheroid shape into semi-toroids capable of more self replication. AI-designed shapes, when built, replicated more often.

Materials and Methods

FAQ, videos, images, and source code can be found at: **krorgs.github.io**

1. Summary of previous work using reconfigurable organisms.

The first manuscript to report reconfigurable organisms (10) introduced a pipeline for automatically designing cardiac-driven organisms to exhibit a desired behavior, such as locomotion. The overall geometry of each organism, and its internal configuration of ectoderm and cardiac muscle, were designed *ab initio* using an evolutionary algorithm and physics-based simulation. The most promising designs were manufactured by combining cells, according to the computer-generated blueprint, and shaping the resultant aggregates with a microcautery electrode and surgical forceps.

Later (9), it was demonstrated that multiciliated epithelial tissue could be used, instead of cardiac muscle, to generate cilia-driven “swimming” designs. These ciliated designs can be manufactured more rapidly and have a higher probability of self motile behavior than the cardiac-driven designs. Ciliated reconfigurable organisms can be produced two different ways. The excised animal cap tissue, including the outer superficial ectodermal layer, can be left intact and allowed to heal into mucociliary epidermal spheroids (Fig. S1*A,B*). Alternatively, if dissociated stem cells from one or more animal caps are brought into contact, they will adhere, compact and reassemble into a mucociliary spheroid (Fig. S1*C,D*). Using either construction method, the resultant aggregates are structurally and functionally equivalent (8). We here refer to these motile spheres as wild type reconfigurable organisms.

Xenopus tissue is ideal for this use case because its cell types and organization are known (43-51) and their development is controllable: cells can be driven to any lineage (52-61) and specific cell types can be inhibited or overproduced with molecular or chemical intervention (62-66). However, outside of (9) and (10), these tissues have not been used as self-motile agents, nor have they been engineered to exhibit specific motile functions such as particle aggregation. In (9), the useful lifespan, velocities, and movements of cilia-driven behavior was quantified as these metrics were not previously reported. These data were used to develop the simulations used in the present work, which builds on both studies to show how ciliated tissues can be shaped to control their collective behavior and amplify their kinematic self replication.

2. The simulation.

This section details how self-replication was simulated. The corresponding Table S1 details how simulation parameters were estimated from biology.

2.1. Biophysics *in silico*.

Voxel-based physics. Biological tissues were modeled as collections of elastic voxels (deformable cuboids) (9,10). Two voxels in the same simulation can connect face to face on a 3D cartesian grid by a single Euler-Bernoulli beam, forming a small body. A beam starts at the center point mass of one voxel and ends at the center of the other voxel. Beams have rotational and translational stiffness allowing for local stretching, compressing, bending, and twisting of one voxel mass relative to another.

Simulated organisms comprise hundreds of voxels. Each voxel within an organism is connected by beams to at most six other voxels, one on each of its six faces (up, down, left, right, front, back). Voxels with less than six beams thus have at least one face that is exposed, forming one part of the external surface of the organism's body (or part of the surface of an internal cavity). Self-collisions between two non-neighboring surface voxels are resolved by temporary beams that are created when two unconnected surface voxels penetrate each other, and are removed after the voxels are pushed far enough apart so that they no longer intersect.

The hydrodynamics of the aqueous medium in which the organisms operate is modeled by a resisting viscous force that damps out inertial effects. Neither laminar nor turbulent flows were simulated. Interactions between voxels and the bottom of the petri dish are modeled as Hookean springs (translational stiffness only), which add an upward force opposing penetration of a surface plane, which is located at z=0 and extends infinitely in the horizontal (x,y) plane. For more details about the underlying physics model, see (40).

GPU acceleration. To simulate the swarms of colliding organisms and dissociated stem cells reported in the present work, we used voxcraft-sim (67), a GPU-accelerated re-implementation of Voxelyze (the physical simulator underpinning VoxCAD (40)) with a more scalable tree-based collision system (68). In Voxelyze, voxels are evaluated sequentially on a single thread of a CPU. In voxcraft-sim, thousands of voxels can be evaluated concurrently on a GPU (Fig. S5). Collisions in Voxelyze are detected and resolved in an exhaustive pairwise comparison of all n surface voxels, with time complexity $O(n^2)$. In voxcraft-sim, collisions are handled using a bounding volume hierarchy (BVH) tree data structure with O(n log n).

Organisms (ciliated, pink voxels). The mature swimming organisms, which are composed of thousands of living cells, are simulated by hundreds of pink colored voxels (Figs. 1*A*, 2*F-H*, S4). Each pink voxel thus approximates a section of tissue, rather than a one-to-one voxel-to-cell representation. The aggregate (metachronal wave) force produced by a patch of beating cilia was modeled on each surface voxel as an impulse force originating at the center of the voxel and pointing in any direction in the horizontal (x,y) plane. The vertical (z) moments and forces of a simulated organism's pink voxels are locked in plane to stabilize their movement and remove the possibility of persistent tumbling behavior *in silico*. Tumbling sometimes does briefly occur in

wild type reconfigurable organisms, but they tend to glide with a constant dorsoventral orientation.

Dissociated stem cells (adhesive, green voxels). Dissociated stem cells are simulated as dissociated (beamless) voxel singletons and are colored green. When two green voxels collide with each other, a new *semi-permanent* beam is created to bond them together. The beam is semi-permanent because it is breakable under conditions that are described below. Green voxels do not have cilia and, unlike pink voxels of the mature organisms, green voxels are free to move and rotate vertically as well as horizontally when hit. In an earlier draft of the model, we simulated dissociated stem cells with negative buoyancy so that they would settle to the bottom of the dish, as observed *in vivo*. However, simulated adhesion under negative buoyancy almost always resulted in flat planes of voxels connected along the surface plane at the bottom of the dish. The model was therefore adjusted so that stem cells were simulated with neutral buoyancy. That is, without collision forces impinging on the green adhesive voxels, they will remain suspended in place. This enabled 3D adhesion because floating voxels are free to rotate out of plane as they bond to other floating voxels and aggregations of voxels.

When dissociated stem cells come together and touch *in vivo* they naturally compact and form spheres as their adhesion properties lead to a minimized surface-area-to-volume ratio. Because our model initially did not capture this spherical bias, green voxels would often connect distally, forming long chains of voxels, which were not observed *in vivo*. To simulate *in vivo* compaction and spherification, piles of connected green voxels are continually compressed together by stochastically detaching the semi-permanent beams of surface voxels that have two or fewer neighbors. When detached from a pile, voxels are immediately pushed toward a different, randomly selected spot along the pile's surface to be reattached upon collision with a new semi-permanent (but breakable) bond. Additional damping was applied to the movement of green voxels to ensure that detached voxels remained within the local neighborhood of a pile.

Petri dish. The depth of the aqueous solution, and its lateral limits (the walls of the dish), were modeled by soft boundaries that repel voxels that penetrate predefined bounds (in the main experiments, a 81 voxel wide[1], 81 voxel long, 5 voxel high volume) with an opposite force proportional to the squared penetration. A hard boundary, such as the surface plane used to model the bottom of the dish, or an upright plane of immovable voxels, could also be used to simulate a wall of a petri dish. However, using fixed voxels for walls has two issues. First, any additional voxels in the simulation require tracking additional collisions which can become computationally expensive. Additionally, the time step of numerical integration must be lowered to prevent simulation instabilities caused by laterally swimming organisms pressing themselves, and piles of simulated stem cells, against a wall of voxels and penetrating it. This can cause the organism or stem cell pile to become permanently bolted to the wall. Finally, we found that hard boundaries, even when computationally stable, biased the random movement of the organisms to remain pressed along the walls of a dish for long intervals of simulation time. While this prediction of wall following was borne out *in vivo*, exhausting a fixed computational budget to collect isolated behavioral data can be wasteful for the purposes of learning to control interactions between organisms and dissociated cells. To reduce the amount of simulation time

[1] Units of distance in the simulation are arbitrary, so the width of a voxel is treated as one unit of distance.

required to observe piling behavior occurring *in silico*, elastic boundaries were implemented which nudge the organisms back toward the dissociated stem cells in the center of the dish.

Hyperparameters. Parameters of the model were estimated from biology according to Table S1. Both the mature organisms' tissue (pink voxels) and the dissociated stem cells (green voxels) were simulated with Young's modulus of 0.05 MPa, density 1000 kg/m^3, and 0.5 Poisson's ratio. These material properties of the voxels were manually adjusted for simulation speed. (Heavier/softer material can be stably simulated with a larger time step of numerical integration because their resonance frequency is lower than light/stiff material.) These properties were kept constant across the two material types to minimize instantaneous changes in dynamics when piles of stem cells develop into ciliated organisms. The development of adhesive, compacting stem cells into the mature tissue of a swimming organism is detailed in the following section.

2.2. Self replication *in silico*.

Filial generations. A swarm of N parent organisms (ciliated pink voxels) were placed amid a uniform lattice of suspended dissociated stem cells (adhesive green voxels). These initial N parents are here referred to as filial generation zero (F0). In the main experiments, there are nine simulated F0 organisms (N=9).

Each filial generation, parents swam for three seconds with random cilia impulse forces, where the x,y cilia force for each surface voxel, in Newtons, was drawn from a bivariate uniform distribution from (-0.3,-0.3) to (0.3,0.3). These cilia forces are held constant, relative to the orientation of the voxel, for one second of simulation time (4676 time steps), yielding ballistic swimming trajectories. After every second of simulation time, all of the cilia forces were replaced by new random values, resulting in three independent random trajectories of collective swimming behavior. As simulated parents swim along the surface of the dish, they collide with the simulated dissociated stem cells, which adhere into piles of stem cells that slowly compact together. At the end of their three second evaluation period, parents were removed from the simulation[2] and the piles were allowed to compact and spherify for an additional 0.5 seconds of simulation time.

The size of the largest pile was then compared against a threshold of 108 voxels, two-thirds the size of the unsculpted, 161-voxel F0 spheres. Piles smaller than the threshold (less than 108 voxels) were removed from simulation, and piles larger than the threshold (if any) develop instantaneously into child organisms with cilia (green voxels become pink voxels) (Fig. S4). This first set of organisms assembled by the F0 parents are referred to as the first filial generation (F1). Empty space in the dish surrounding the F1 organisms (due to the removal of parents and small piles below the threshold) is repopulated by a fresh grid of dissociated stem cells, and a new 3.5 second evaluation period begins in which the F1 organisms are the pile-building parents.

The F1 organisms may build piles, the largest of which may develop into F2 organisms, which in turn may build piles of their own, and so on. The simulation ends when no parents (pink voxels) remain in the dish, or after a maximum of five filial generations (F5) elapse, for at most 6*3.5 = 21 seconds.

[2] The parents could be left in the dish *in vivo* as they maintain self motility for 10 days without additional food (90 days with food) and it only takes four days for a pile of stem cells to develop into a ciliated spheroid and begin moving. However, the parents are removed in order to isolate the pile-making capacity of each filial generation.

Hyperparameters. The behavior of each filial generation was simulated for 16,366 time steps (just long enough to see pile-making behavior occur), with step size 2.14×10^{-4} sec (just low enough to ensure simulation stability; for details see (40)), yielding an evaluation period of 3.5 simulation seconds. Table S1 details how these simulated dynamics correspond to properties of the physical self-replicating system, *in vivo*.

3. The AI design tools.

This section describes how parameters of reconfigurable organisms, and their environment, can be adjusted to generate a desired amount of kinematic self replication in reconfigurable organisms.

3.1. Controllability of reconfigurable organisms.

Individual behavior. Previous work (10) used an evolutionary algorithm to automatically design the overall shape, and distributions of epidermal and cardiac tissues, of deciliated reconfigurable organisms, so that they would exhibit some desired behavior such as surface-based locomotion in a specified direction. Behavior generated in simulation was observed in some of the manufactured organisms because cardiac-driven movement was sufficiently determined by geometry and tissue distribution. The behavior of the cilia-driven swimming organisms manufactured here, in contrast, are not as obviously determined by their geometry: very similarly shaped bodies can move very differently. Even a single organism can exhibit diverse movement patterns driven by spontaneous transitions in cilia beating patterns, rather than traveling along a single trajectory as when driven by a regular cardiac pulse.

Collective Behavior. Predicting cilia-driven movement of an individual organism is challenging. But some collective behaviors do appear to be predictable in simulation. Specifically, it was found that when a swarm of ciliated reconfigurable organisms are placed together in the same dish amid debris [carmine dye particles (10) or silicone coated iron oxide beads (9)], they tend to reliably aggregate the initially scattered debris into piles. Previous modeling studies (9) assessed whether body shape could affect pile size *in silico* under precisely tuned movement trajectories (a custom set of static cilia forces was optimized for each swarm to increase pile size). The data suggested that some body shapes were capable of building significantly larger piles than others, but this hypothesis was not verified *in vivo*. And because the simulated debris were intended to model synthetic material, piles of debris did not develop into child organisms. In previous implementations of dynamic voxel attachment, piles were only numerically stable if inertial forces were heavily overdamped post-attachment, resulting in heavy, irregularly-shaped masses of tangled voxels that could not stably locomote using cilia impulse forces.

The “debris” in this present work, instead, are dissociated stem cells that, when pushed together into a sufficiently large pile, compact and develop into a ciliated organism (offspring) capable of swimming and pushing together loose stem cells into additional piles (which can then develop into yet additional offspring). The control problem is thus to adjust the amount of self

replication produced by the swarm without knowing exactly how the individual organisms will move.

3.2. Increasing the amount of self replication.

There are various adjustable parameters of the self reproducing system that can be manually tuned or tuned by an evolutionary algorithm (Table S1) to affect the amount of self replication.

Some of these conditions are strict and non-adjustable. Contamination, for instance, must be avoided or viability will be lost between rounds of replication. Likewise, a suitable temperature range for frog embryos and *ex vivo* tissues/cells must be maintained *in vitro* (4°C to 28°C). Other conditions are more adjustable. For instance, the size of the petri dish and the number of organisms could be changed. The size of the manually constructed organisms are all 400-600 microns in diameter (Fig. S3), but can be made larger or smaller (Fig. S1). The adherence properties of the dissociated stem cells could be altered through the expression of cadherins or integrins. Reconfigurable organisms live for 10 to 14 days from the energy preloaded in their cells; but they can survive for at least three months in a nutrient rich medium (9). The speed at which the organisms can move during their lifetimes can be throttled by increasing or decreasing the viscosity of their aqueous environment and the friction of the arena substrate. The structure of the bottom surface or walls of the dish can channel and/or constrain the otherwise unpredictable movement of cilia-driven reconfigurable organisms (9). Finally, the morphology of the organisms can affect how they interact with other objects and with each other (9,10). This inherent sensitivity of kinematic self replication to adjustable external conditions exposes several potential control parameters that can be set by a human operator or automatic control system.

Here, we focus on two such parameters: the shape of the organisms and the structure of the terrain on which they operate.

Body shape. The initial swarm of reconfigurable organisms (F0), which are formed by manually deconstructing one-day old Xenopus embryos, naturally compact into spheroids due to cell adherence (referred to here as “wild type”), but they can be carved into other shapes by subtraction (Fig. S1F,H). The wild type F0 spheroids are here modeled as a vertical stack of five circular layers of 21, 37, 45, 37, and 21 voxels, respectively, yielding a voxelized spheroid composed of 161 voxels with a 7:5 width:height aspect ratio (Fig. S4). Other body shapes can be formed by removing one or more of the 161 voxels in a single simulated spheroid. For simplicity, each of the N organisms within a swarm were constrained to share the same body shape.

Terrain (black voxels). The terrain of a simulated petri dish can be modified by adding fixed structures along the bottom surface of the dish, in the form of black voxels. Because the simulated organisms cannot move over or through the fixed structures, the terrain can channel the random movement of the organisms along more predictable trajectories within predefined limits. Details of the two experiments modifying body shape and terrain, respectively, are identical unless stated otherwise.

Encoding shape. A structure made of voxels (whether body shape or terrain) can be encoded as a network that takes as input a set of regularly-spaced coordinates within a bounding volume of fixed size, and outputs whether or not a voxel is present at each of those

three-dimensional locations. Consistent with previous computational models of reconfigurable organisms (10), a feedforward Compositional Pattern-Producing Network, or CPPN (39), was used to encode voxel structures. A CPPN consists of vertices connected by weighted edges. Each edge multiplies its input value by a real valued weight between -1 and 1. Each vertex sums the values of its input edges and outputs a function applied to that sum. The function encoded in a node is drawn from the following set: sine, signum, square, absolute value, square root of the absolute value; and the negations of those five functions. In the last layer of the network, positive output values correspond to present voxels and negative values correspond to empty space (an additional signum function is applied). The largest connected component of voxels was taken to be the structure. Alteration to edge weights and/or changes in node-encoded functions alters the structure output by the network. For more details, see (69).

When encoding body shape, for the main experiments within a flat petri dish, networks were restricted to removing vertical columns of voxels along the z axis, at particular positions in (x,y), from the default spheroid, rather than removing individual voxels. This ensured that, if a simulated shape were to be instantiated as a physical reconfigurable organism, organisms could be rapidly shaped using coarse subtraction, instead of sculpting intricate 3D concavities into each one (10). Similarly, when encoding terrain, only one-voxel tall structures (z=0) were considered so that all of the immovable black voxels rested on the bottom of the dish. Thus, in both cases, only the x and y coordinates need to be input to the encoding network.

Measuring the amount of self replication. The amount of self replication achieved by a specific body shape or terrain can be measured by the number of filial generations (g) they generate. The fitness, f, of a CPPN is computed as:

$$f = s/p + g \,, \qquad \text{(Eqn. 1)}$$

where s is the size of the largest pile (the number of voxels it contains) at the end of the evaluation period; p is the pile size threshold required for a pile to develop into an organism (if s is greater than p, a new filial generation begins, otherwise the evaluation period ends); and g is the number of filial generations achieved. A conservative threshold (s = 108 voxels) of two-thirds the size of the simulated wild type spheres (161 voxels) was selected such that relatively few randomly generated swarms achieved $g > 0$. This significantly reduced the computational effort required to find viable terrains and body shapes that increase the amount of self replication. It also matched the observation that physical swarms composed of the wild type spheroids usually only managed one generation of replication.

Optimization algorithm. CPPNs were optimized to output replicator shapes, or terrains, that cause more self replication than that observed in the wild type spheroids. An evolutionary algorithm was used because the authors have considerable experience using this particular algorithm to evolve soft robots and reconfigurable organisms in previous work. Many optimization methods could be adapted for optimizing CPPNs, but derivative-free optimization methods such as evolutionary algorithms are a natural choice for this problem because the relationship between behavior and morphology was modeled using a nondifferentiable physical simulator. More specifically, low self replicative ability cannot yet be localized to specific missing parts of specific piles. These missing pile parts in turn cannot yet be propagated back through the physical simulator to implicate movement patterns of specific swarm members, and

back further to specific parts of the replicators' bodies causing those movements. Finally, implicated body parts cannot be propagated back further into the CPPN, to implicate specific edges and nodes that should be tuned to rectify the low replicative ability. In addition, evolutionary rather than learning algorithms are desirable because initial conditions of the system (body shapes, terrains) are optimized here, rather than optimizing the control of each organism.

The evolutionary algorithm used here is a multiobjective optimization algorithm (38) that continuously injects new design alternatives into the population, and reduces selection pressure on newer designs, in order to favor the evolution of new, different ways to achieve self replication. Each independent evolutionary trial starts with its own unique set of 16 initially random CPPNs, and a sequence of random (but static) cilia forces (described in Sect. S2.1). Each CPPN is translated into a swarm, or a terrain for the default swarm of spheroids. The swarm is simulated and its self replicative ability is measured. A modified copy is made of all 16 CPPNs in the population, and each copy inherits the lineage age of its parent CPPN. A mutation adds, removes, or modifies one of the network's edges or vertices. Vertex modification involves replacing the activation function currently encoded there with a function randomly selected from the following set: sine, signum, square, absolute value, square root of the absolute value. The age of each of the 32 CPPNs is incremented by one, and one new CPPN with a lineage age of zero is randomly generated. The 17 new swarms produced by the 17 new CPPNs are evaluated *in silico,* as described in Sect. S2.2. Then, the entire population of 16+17=33 CPPNs are then sorted, on the basis of their age and fitness scores (Eqn. 1), into Pareto fronts. The first Pareto front consists of the youngest and most fit CPPNs, which are by definition nondominated. The second Pareto front consists of CPPNs that are dominated by at least one CPPN in the first front, but are not dominated by any other CPPNs. The N-th front consists of CPPNs that are dominated only by CPPNs the preceding N-1 fronts. Starting with the first Pareto front, successive fronts are kept in their entirety until doing so would overfill the population past its original size, 16 CPPNs, at which point CPPNs are added stochastically with probability proportional to their fitness until the population contains 16 CPPNs.

When evolving body shape, 49 independent evolutionary trials were conducted. Each evolutionary trial started with its own unique set of random shape-encoding CPPNs and sets of random cilia forces, yielding 49 champion swarms: the body shape that achieved the highest value of Eqn. 1 above, in each trial.

Runtime. Each evolutionary trial was conducted using eight NVIDIA Tesla V100s for a maximum of 48 hours wall-clock time or 500 updates of the CPPN population (whichever came first). The runtime varies due to the algorithm's stochasticity; some swarms produce more filial generations than others and thus require more time to simulate. Because evaluating swarms in simulation is the computational bottleneck, the algorithm is readily parallelizable: doubling the number of GPUs would allow halving the wall-clock time for the same population size, or doubling the size of the CPPN population that can be evaluated using the same amount of wall-clock time.

3.3. Inhibiting and recovering self replication.

A simple way to stop kinematic self replication is to stop supplying the system with additional building materials (here, dissociated stem cells). This is one of the reasons that

kinematic self replication is inherently more controllable than the other nine known forms of biological replication. Another way to slow or halt a kinematic self-replicator is to impede its movement in a cluttered environment.

Cluttered environment. To investigate whether the evolutionary algorithm could impart self replication to a system otherwise incapable of it, a cluttered environment was created by attaching a sparse uniform grid of immovable black voxels to the bottom of the dish (Fig. S9). The simulated wild type reconfigurable organisms could no longer spontaneously self-replicate in this environment because their movement is contained within a small region surrounding their starting position (Fig. S9A). However, if sections are removed from the simulated organisms' ventral surfaces, they can glide over the top of the static debris (Fig. S9B-D). The challenge here is to not only regain movement, but to recover self replication. This requires carving away voxels on the ventral surface of a body shape while retaining the ability to capture and aggregate dissociated cells into piles. Thus, instead of carving away entire columns at a time (which simplifies manufacture), independent removal of any voxel within the sphere was permitted.

4. Statistical analysis.

4.1. Size of offspring.

In silico. Five hundred simulations were conducted in which two groups— the wild type spheroids and the evolved semitoroids—built piles. In each simulation, the swarm moved differently, as each member was driven by different random cilia forces. The simulations were terminated before any piles could develop into F1 organisms. The null hypothesis is that the average size of the piles built by the spheroids was no different from the size of those built by the optimized shape (the semi-torus). Because the same random cilia forces were used for the spheres and the evolved shape, the two samples are dependent. Thus, a Wilcoxon test was performed, resulting in $p=3.9*10^{-5}$ (W=6311.5). Controlling for false discovery rate, the null hypothesis is rejected at the 0.0001 level of significance.

In vivo. The sizes of the 10 largest physical F1 offspring generated by each of eight different swarms was recorded. Five of the swarms were composed of wild type spheroids, one was composed of spheroids double the size, and one was composed of flattened spheroids (gray points in Fig. 2E). Each swarm behaved within a dish with differing dissociated cell density. The sizes of the 10 largest physical F1 offspring generated by each of three additional swarms, composed of the automatically designed semitoroid, were also recorded, again at different dissociated cell densities (pink points in Fig. 2E). Within each set of 10, the size of the offspring was divided by the cell density in which they were built. The null hypothesis is that the average diameter of the offspring (normalized by cell concentration) built by semitoroids progenitors across three independent trials was no different than the average diameter of the offspring built across five independent trials by the wild type spheroids or spheroid variants. Comparing offspring size in this way is a conservative test since the volumetric difference between two spheres is eight times as large as their corresponding difference in diameter. A Mann Whitney U test was performed, resulting in $p=0.0368$ (U=1.0). Controlling for false discovery rate, the null hypothesis is rejected at the 0.05 level of significance.

4.2. Number of generations.

In silico. The 49 evolutionary trials resulted in progenitor shapes that self-replicated for two to three generations *in silico*, under strict conditions: a pile size threshold of two thirds the number of voxels contained within the simulated wild type spheres. Two thirds is a strict threshold because the best estimate is closer to one fourth (see Table S1). All 49 trials were compared to evaluations of spheres. The wild type spheres did not self replicate for more than a single generation, in any of the 49 trials. Bootstrapped confidence intervals of the 49 best swarms from each trial were compared against 49 of the wild type spheroid swarms to determine the probability of overlap (Fig. S6A). Controlling for false discovery rate the null hypothesis is rejected at the 0.0001 level of significance.

The same procedure was performed for terrain optimization with wild type spheroid swarms *in silico* (Fig. S7). The null hypothesis is that of no difference in the number of filial generations produced by swarms operating on the best evolved terrains (e.g. Fig. S8) and those operating on the flat surface plane of a standard petri dish (e.g. Fig. S4). Based on the bootstrapped confidence intervals, and controlling for false discovery rate, the null hypothesis is rejected at the 0.0001 level of significance.

In vivo. The wild type reconfigurable organisms produced just a single filial generation in four of the five independent trials. The only trial to produce two generations of offspring required the highest cell concentration we tested (150 cells/mm^2). In the first of three self replication trials using the optimized body shape (semitoroids) resulted in two generations at 61 cells/mm^2 but then degraded into immobility due to a fungal infection. In the second and third trials using the optimized body shape, additional precautions were taken to avoid fungal infections. Three successive generations of offspring were produced at 61 cells/mm^2; four successive generations of offspring were produced at 91 cells/mm^2. The null hypothesis is that the number of generations of self replication achieved by the optimized design (2g, 3g, 4g) was no greater than the number of generations produced by the wild type spheroids (1g, 1g, 1g, 1g, 2g). A Mann Whitney U test was performed: p=0.0188. (U=0.5). Controlling for false discovery rate, the null hypothesis is rejected at the 0.05 level of significance.

4.3. Correlation between first generation size and total number of generations *in vivo*.

There was a Spearman rank-order correlation coefficient of 0.9322 (p=0.00074) between the number of replication generations achieved and the aggregate size of the 10 largest first generation offspring.

5. Utility forecast.

A computational model was created to predict the amount of utility (useful work) the self-replicating swarm may be capable of, if it was provided with reachable but unassembled parts in a semi-structured environment. To that end, a circuit completion task was chosen. This section details how the parameters were estimated for the self-replicating swarm and the electronic parts. The model incorporates many biological details from the physical

reconfigurable organisms reported here, and from emerging microscale electronic components. But, many of the details estimated in the model will be refined when more is known about how such organisms can or cannot interact with various microscale environments containing artificial materials. This will, in future, yield better forecasts of the potential utility of this technology.

5.1. Circuit components.

Three types of modular microelectronic components were simulated: light emitters, batteries, and wire. Each component contains vertically stacked and insulated conductors, which maintains connectability under translational and rotational movement in plane (Fig. S11*C-E*). That is, the electronic components, if resting on a surface plane, can be pushed together and connected by a swarm of reconfigurable organisms that move along the same surface. The simulated wires (blue voxels in Fig. S11*A*) adhere to each other upon collision like the simulated dissociated stem cells do (green voxels). Except, once the wires attach, they do not detach (there is no stochastic spherification as in the stem cells). Current emanates from a power source that could, if instantiated physically, be supplied by a microbattery or electrodes, and is approximated in simulation by passing discrete packets of voltage along neighboring voxels in a chain of connected voxels. If a packet of voltage reaches a light emitter, it is switched on, permanently.

There exist atomically-thin light emitters with light emission visible to the naked eye that are made of just a few layers of graphene, stretched across a 2D sheet <5 μm in length and width and powered at ~0.4 V μm^{-1} (27). Any organisms gathering and connecting these emitters to a power supply would have to be removed or sacrificed before powering the circuit. The number of switched-on light emitters was chosen here as the unit of "useful work" performed by a self-replicating swarm, but the choice was arbitrary. There are other kinds of microscale resistors, such as transistors, which could be used instead, or any number of other kinds of microscale inspection, maintenance or assembly tasks.

5.2. Estimated utility.

Task environment. Sixteen initially disconnected strips of vertically stacked and insulated conductive voxels ("wires"; blue voxels) are spread out along the edge of the soft boundary of a simulated dish (Figs. 4 and S11). In each corner, two of the strips are connected at a 90 degree angle to a small light emitter (white voxels). Two of the remaining eight strips along the edge, on opposing sides, are attached to power supplies. Nine reconfigurable organisms are placed in the center of the simulated dish amid a grid of dissociated stem cells. Twelve additional strips of vertically-insulated conductive voxels are placed among them, randomly oriented north-south or east-west with equal probability (Fig. 4*B,C*). Potential current flow is shown in yellow propagating down blue conductive voxels connected to a power supply. As organisms move in their dish, they self replicate (by building piles out of dissociated stem cells) and, simultaneously, snap together the conductive strips of voxels in the dish as a side effect of movement. If one of the corner strips with a light emitter connects by conductive voxels to one of the two power supplies, the light emitter switches on (as indicated by a red circled X in Figs. 4 and S11).

The swarm builds piles, which, if sufficiently larger than 40 voxels, develop into offspring, and the dissociated cells are replenished, every 3.5 seconds, as in the above experiments. Forty voxels is one fourth the size of the simulated wild type spheroids, which is the best estimate for

the minimum size of piles that developed into self motile offspring *in vivo* (Table S1). Because utility is measured rather than self replication, the parents are left in the dish and continue building additional filial generations alongside their offspring for 17.5 seconds.[3] As the organisms move they randomly push the circuit components into place, occasionally turning on up to four light emitters. After 17.5 seconds of simulation time, the parents were removed, and the offspring were extracted. To better approximate the spherification that occurs *in vivo*, offspring extracted from a completed simulation are converted to spheroids containing roughly the same number of voxels. The spherified offspring were then split into two subgroups, each subgroup was injected into one of two new simulated petri dishes, and each new dish contains a new partially-completed circuit. Self replication and circuit building begin afresh in these two dishes, again for 17.5 seconds. This process triggers the growth of a binary simulation tree (Fig. 4) in which each simulation begets at most two simulation branches, each containing one half of the produced offspring of their root simulation. If only a single offspring is created by a swarm after 17.5 seconds, then only one new simulation branch is spawned. If no offspring were built, then that branch of the binary simulation tree dies out.

Growth rate of utility. After 50 simulation bifurcations (875 seconds of simulation time), 5024 light emitters were switched on by the self-replicating swarm.

Symbolic regression (42) was used to find the degree of a polynomial function that best explains the cumulative number of emitters switched on by the self-replicating swarm. The regression operators were limited to addition and multiplication. The operands were the number of simulation bifurcations (a sequence from 1 to 51), and an ephemeral constant drawn from a gaussian distribution (mu=0, sigma=10). Each candidate solution is evaluated based on its root mean squared error (RMSE) with the cumulative number of emitters switched on at each simulation bifurcation.

A population of 1000 candidate equations was optimized for 1000 generations using the same optimization algorithm (38) used to design body shapes and terrains. The population size could be set much larger for this experiment because evaluating equations takes milliseconds whereas evaluating self-replicating swarms takes minutes. Ten independent optimization trials were conducted, each starting from a different random set of 1000 candidate equations. The objective is to minimize root mean squared error. After 1000 generations, the least-error equations found in each trial all converged about the quadratic curve derived by ordinary least squares: $2.7x^2 - 43x + 182.4$, where x is the number of simulation bifurcations (R^2=0.9988). The prediction of the model is thus, under the simulated conditions, utility increases quadratically with time.

Self replication (and thus utility) could, in principle, be enhanced *in vivo* through numerous bioengineering and molecular interventions, including: altering cell adherence properties (through the expression of cadherins or integrins), increasing cell lifespan with culture media, increasing swimming velocity by altering the number and polarity of cilia, changing cilia beat frequency, generating larger parents, increasing the number of adults during self replication, provision of more feeder cells, altering the size of the arena, and changing the substrate on which self replication occurs (increased or decreased friction). For the current settings of these

[3] The organisms can survive 10-14 days without food, consuming the energy preloaded in the frog egg (similar to the yolk of a chicken egg). If given an external food source, in the form of a sugar rich media, they can survive for a period of months.

parameters, and others that could affect the rate of utility produced by future reconfigurable organisms, see Table S1.

It is clear that, in theory, self-replicative machines that perform useful work as a side effect will superlinearly increase in utility over time. However, it was not clear that there exists a domain in which the randomly-acting self-replicative system described here would be so. The flexible electronics technology simulated here demonstrates that, assuming such technology comes to fruition, there may soon be a domain in which our technology may be superlinearly useful over time.

Supplemental References

1. Kamm, R.D., Bashir, R., Arora, N., Dar, R.D., Gillette, M.U., Griffith, L.G., Kemp, M.L., Kinlaw, K., Levin, M., Martin, A.C. and McDevitt, T.C. Perspective: The promise of multi-cellular engineered living systems. *APL Bioengineering*, **2**, 040901 (2018).
2. Garreta, E., Kamm, R.D., de Sousa Lopes, S.M.C., Lancaster, M.A., Weiss, R., Trepat, X., Hyun, I. and Montserrat, N. Rethinking organoid technology through bioengineering. *Nature Materials*, **20**, 145-155 (2021).
3. Huh, D., Matthews, B.D., Mammoto, A., Montoya-Zavala, M., Hsin, H.Y. and Ingber, D.E. Reconstituting organ-level lung functions on a chip. *Science* **328**, 1662-1668 (2010).
4. Wu, Q., Liu, J., Wang, X., Feng, L., Wu, J., Zhu, X., Wen, W. and Gong, X. Organ-on-a-chip: Recent breakthroughs and future prospects. *Biomedical Engineering Online*, **19**, 1-19 (2020).
5. Losner, J., Courtemanche, K. & Whited, J.L. A cross-species analysis of systemic mediators of repair and complex tissue regeneration. *npj Regen Med* **6**, 21 (2021).
6. Hussey, G.S., Dziki, J.L. and Badylak, S.F. Extracellular matrix-based materials for regenerative medicine. *Nature Reviews Materials*, **3**, 159-173 (2018).
7. Han, Y., Li, X., Zhang, Y., Han, Y., Chang, F. and Ding, J. Mesenchymal stem cells for regenerative medicine. *Cells*, **8**, 886 (2019).
8. Gilbert, S.F., Sarkar, S. Embracing complexity: organicism for the 21st century. *Developmental Dynamics*, **219**, 1-9 (2000).
9. Blackiston, D., Lederer, E., Kriegman, S., Garnier, S., Bongard, J., Levin, M. A cellular platform for the development of synthetic living machines. *Science Robotics* **6**, eabf1571 (2021).
10. Kriegman, S., Blackiston, D., Levin, M., Bongard, J. A scalable pipeline for designing reconfigurable organisms. *Proceedings of the National Academy of Sciences* **117**, 1853-1859 (2020).
11. Jones, E. A., & Woodland, H. R. Development of the ectoderm in Xenopus: tissue specification and the role of cell association and division. *Cell*, **44**, 345-355 (1986).

12. Kim, H. Y., Jackson, T. R., Stuckenholz, C., Davidson, L. A. Tissue mechanics drives regeneration of a mucociliated epidermis on the surface of Xenopus embryonic aggregates. *Nature Communications*, **11**, 1-10 (2020).

13. Walentek, P. Manipulating and analyzing cell type composition of the Xenopus mucociliary epidermis. *Xenopus*, 251-263 (2018). Humana Press, New York, NY.

14. Stubbs, J. L., Davidson, L., Keller, R., Kintner, C. Radial intercalation of ciliated cells during Xenopus skin development. *Development*, **133**, 2507-2515 (2006).

15. von Neumann, J. Theory of self-reproducing automata, Ed. Burks, A.W., *University of Illinois Press* (1966).

16. Ray, T.S., Evolution, complexity, entropy and artificial reality. *Physica D: Nonlinear Phenomena*, **75**, 239-263 (1994).

17. Chou, H.H. and Reggia, J.A. Emergence of self-replicating structures in a cellular automata space. *Physica D: Nonlinear Phenomena*, **110**, 252-276 (1997).

18. Studer, G. and Lipson, H. Spontaneous emergence of self-replicating structures in molecube automata. In Proc. of *the 10th Int. Conf. on the Simulation and Synthesis of Living Systems*, 227-233 (2006).

19. Penrose, L. S. Self-reproducing machines. *Scientific American*, **200**, 105-117 (1959).

20. Jacobson, H. On models of reproduction. *American Scientist*, **46**, 255-284 (1958).

21. Chirikjian, G. S., Zhou, Y., Suthakorn, J. Self-replicating robots for lunar development. *IEEE Transactions on Mechatronics*, **7**, 462-472 (2002).

22. Zykov, V., Mytilinaios, E., Adams, B., Lipson, H. Self-reproducing machines. *Nature*, **435**, 163-164 (2005).

23. Griffith, S., Goldwater, D. & Jacobson, J. Self-replication from random parts. *Nature*, **437**, 636 (2005).

24. Adams, B. and Lipson, H. A universal framework for analysis of self-replication phenomena. *Entropy*, **11**, 295-325 (2009).

25. Chirikjian, G. S. Parts entropy and the principal kinematic formula. In Procs. of *the IEEE Intl. Conf. on Automation Science and Engineering*, 864-869 (2008). 10.1109/COASE.2008.4626465

26. Qu, Zhe, et al. Towards high-performance microscale batteries: Configurations and optimization of electrode materials by in-situ analytical platforms. *Energy Storage Materials*, **29**, 17-41 (2020).

27. Kim, Y., Kim, H., Cho, Y. et al. Bright visible light emission from graphene. *Nature Nanotech* **10**, 676–681 (2015).

28. Gao, W., Ota, H., Kiriya, D., Takei, K., & Javey, A. Flexible electronics toward wearable sensing. *Accounts of Chemical Research*, **52**, 523-533 (2019).

29. Ricotti, L., Trimmer, B., Feinberg, A.W., Raman, R., Parker, K.K., Bashir, R., Sitti, M., Martel, S., Dario, P. and Menciassi, A. Biohybrid actuators for robotics: A review of devices actuated by living cells. *Science Robotics*, **2**, eaaq0495 (2017).

30. Park, S.J., Gazzola, M., Park, K.S., Park, S., Di Santo, V., Blevins, E.L., Lind, J.U., Campbell, P.H., Dauth, S., Capulli, A.K. and Pasqualini, F.S., Phototactic guidance of a tissue-engineered soft-robotic ray. *Science*, **353**, 158-162 (2016)

31. Maury, C. P. J. Amyloid and the origin of life: self-replicating catalytic amyloids as prebiotic informational and protometabolic entities. *Cellular and Molecular Life Sciences*, **75**, 1499-1507 (2018).

32. Tank, E. M., Harris, D. A., Desai, A. A., & True, H. L. Prion protein repeat expansion results in increased aggregation and reveals phenotypic variability. *Molecular and Cellular Biology*, **27**, 5445-5455 (2007).

33. Boer, M.M., de Dios, V.R. and Bradstock, R.A. Unprecedented burn area of Australian mega forest fires. *Nature Climate Change*, **10**, 171-172 (2020).

34. Emanuel, K. Increasing destructiveness of tropical cyclones over the past 30 years. *Nature*, **436**, 686-688 (2005).

35. Lin, N., Kopp, R.E., Horton, B.P. and Donnelly, J.P. Hurricane Sandy's flood frequency increasing from year 1800 to 2100. *Proceedings of the National Academy of Sciences*, **113**, 12071-12075 (2016).

36. Liu, Y.Y., Slotine, J.J. and Barabási, A.L. Controllability of complex networks. *Nature*, **473**, 167-173 (2011).

37. Nieuwkoop, P. D., & Faber, J. Normal table of. Xenopus laevis, **252** (1994).

38. Schmidt, M., Lipson, H. Age-fitness pareto optimization. *Genetic Programming Theory and Practice VIII*, 129-146 (2011).

39. Stanley, K. O. Compositional pattern producing networks: a novel abstraction of development. *Genetic Programming and Evolvable Machines* **8**, 131-162 (2007).

40. Hiller, J. and Lipson, H. Dynamic simulation of soft multimaterial 3D-printed objects. *Soft Robotics*, **1**, 88-101 (2014).

41. Benjamini, Y. , Hochberg, Y. Controlling the false discovery rate: A practical and powerful approach to multiple testing. *Journal of the Royal Statistical Society: Series B (Methodological)*, **57**, 289-300 (1995).

42. Schmidt, M., Lipson, H. Distilling free-form natural laws from experimental data. *Science*, **324**, 81-85 (2009).

43. Müller, H. A. J., Hausen, P. Epithelial cell polarity in early Xenopus development. *Developmental Dynamics*, **202**, 405-420 (1995).

44. Deblandre, G. A., Wettstein, D. A., Koyano-Nakagawa, N., Kintner, C. A two-step mechanism generates the spacing pattern of the ciliated cells in the skin of Xenopus embryos. *Development*, **126**, 4715-4728 (1999).

45. Werner, M. E., Mitchell, B. J. Understanding ciliated epithelia: the power of Xenopus. *Genesis*, **50**, 176-185 (2012).

46. Walentek, P., Bogusch, S., Thumberger, T., Vick, P., Dubaissi, E., Beyer, T., Blum, M. and Schweickert, A. A novel serotonin-secreting cell type regulates ciliary motility in the mucociliary epidermis of Xenopus tadpoles. *Development*, **141**, 1526-1533 (2014).

47. Dubaissi, E., Rousseau, K., Lea, R., Soto, X., Nardeosingh, S., Schweickert, A., Amaya, E., Thornton, D.J., Papalopulu, N. A secretory cell type develops alongside multiciliated cells, ionocytes and goblet cells, and provides a protective, anti-infective function in the frog embryonic mucociliary epidermis. *Development*, **141**, 514-1525 (2014).

48. Walentek, P., & Quigley, I. K. What we can learn from a tadpole about ciliopathies and airway diseases: Using systems biology in Xenopus to study cilia and mucociliary epithelia. *Genesis*, **55**, e23001 (2017).

49. Kim, S. K., Zhang, S., Werner, M. E., Brotslaw, E. J., Mitchell, J. W., Altabbaa, M. M., Mitchell, B. J. CLAMP/Spef1 regulates planar cell polarity signaling and asymmetric microtubule accumulation in the Xenopus ciliated epithelia. *Journal of Cell Biology*, **217**, 1633-1641 (2018).

50. Angerilli, A., Smialowski, P., & Rupp, R. A The Xenopus animal cap transcriptome: building a mucociliary epithelium. *Nucleic Acids Research*, **46**, 8772-8787 (2018).

51. Chuyen, A., Rulquin, C., Daian, F., Thomé, V., Clément, R., Kodjabachian, L., Pasini, A. The Scf/Kit pathway implements self-organized epithelial patterning. *Developmental Cell*, **56**, 795-810 (2021).

52. Green, J. B., Smith, J. C. Graded changes in dose of a Xenopus activin A homologue elicit stepwise transitions in embryonic cell fate. *Nature*, **347**, 391-394 (1990).

53. Thomsen, G., Woolf, T., Whitman, M., Sokol, S., Vaughan, J., Vale, W., Melton, D. A. Activins are expressed early in Xenopus embryogenesis and can induce axial mesoderm and anterior structures. *Cell*, **63**, 485-493 (1990).

54. Thomsen, G. H., Melton, D. A. Processed Vg1 protein is an axial mesoderm inducer in Xenopus. *Cell*, **74**, 433-441 (1993).

55. Gurdon, J. B., Harger, P., Mitchell, A., Lemaire, P. Activin signalling and response to a morphogen gradient. Nature, **371**, 487-492 (1994).

56. Ariizumi, T., Asashima, M. In Vitro Control of the Embryonic Form of Xenopus laevis by Activin A: Time and Dose‐Dependent Inducing Properties of Activin‐Treated Ectoderm: (activin/ectoderm/organizer/Xenopus laevis/neural induction). *Development, Growth & Differentiation*, **36**, 499-507 (1994).

57. Sasai, Y., Lu, B., Piccolo, S., De Robertis, E. M. Endoderm induction by the organizer‐secreted factors chordin and noggin in Xenopus animal caps. *The EMBO Journal*, **15**, 4547-4555 (1996).

58. Miyanaga, Y., Shiurba, R., Asashima, M. Blood cell induction in Xenopus animal cap explants: effects of fibroblast growth factor, bone morphogenetic proteins, and activin. *Development Genes and Evolution*, **209**, 69-76 (1999).

59. Ariizumi, T., Takahashi, S., Chan, T. C., Ito, Y., Michiue, T., Asashima, M. Isolation and differentiation of Xenopus animal cap cells. *Current Protocols in Stem Cell Biology*, **9**, 1D-5 (2009).

60. Ariizumi, T., Michiue, T., Asashima, M. In Vitro Induction of Xenopus Embryonic Organs Using Animal Cap Cells. *Cold Spring Harbor Protocols*, pdb-prot097410 (2017).

61. Teegala, S., Chauhan, R., Lei, E., Weinstein, D. C. Tbx2 is required for the suppression of mesendoderm during early Xenopus development. *Developmental Dynamics*, **247**, 903-913 (2018).

62. Marnellos, G., Deblandre, G. A., Mjolsness, E., Kintner, C. Delta-Notch lateral inhibitory patterning in the emergence of ciliated cells in Xenopus: experimental observations and a gene network model. In *Biocomputing 2000*, 329-340 (1999).

63. Stubbs, J. L., Oishi, I., Belmonte, J. C. I., Kintner, C. The forkhead protein Foxj1 specifies node-like cilia in Xenopus and zebrafish embryos. *Nature Genetics*, **40**, 1454-1460 (2008).

64. Quigley, I. K., Stubbs, J. L., Kintner, C. Specification of ion transport cells in the Xenopus larval skin. *Development*, **138**, 705-714 (2011).

65. Myers, C. T., Appleby, S. C., Krieg, P. A. Use of small molecule inhibitors of the Wnt and Notch signaling pathways during Xenopus development. *Methods*, **66**, 380-389 (2014).

66. Brooks, E. R., Wallingford, J. B. Multiciliated cells. *Current Biology*, **24**, R973-R982 (2014).

67. Liu, S., Matthews, D., Kriegman, S., Bongard, J. Voxcraft-sim, a GPU-accelerated voxel-based physics engine. 10.5281/zenodo.3835152, https://github.com/voxcraft/voxcraft-sim (2020).

68. Karras, T. Maximizing parallelism in the construction of BVHs, octrees, and k-d trees. In *Procs. of the ACM Conf. on High-Performance Graphics*, 33-37 (2012).

69. Cheney, N., et al. Unshackling evolution: Evolving soft robots with multiple materials and a powerful generative encoding." In Procs. of the Genetic and Evolutionary Computation Conf. (2013).

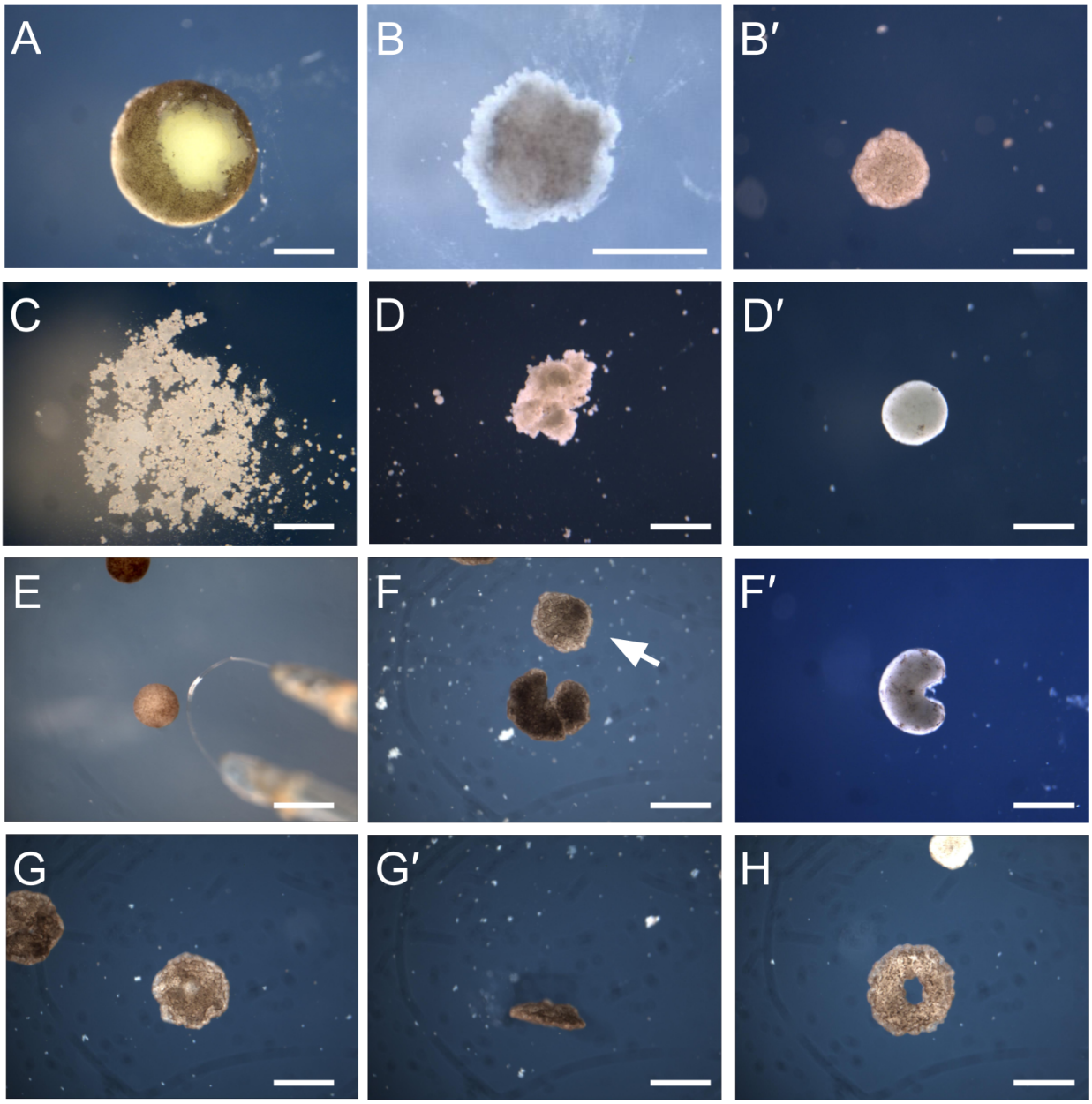

Fig. S1. Construction of reconfigurable organisms from embryonic *Xenopus* material. Two methods are used to construct the initial swarm (generation 0) of reconfigurable organisms. The first requires excision of animal cap tissue of Nieuwkoop and Faber stage 10 embryos (24h post fertilization at 14°C) with microsurgery forceps (**A**). Individual explants are then transferred to a 0.75x saline solution (Marc's Modified Ringer's) which allows the tissue to heal into a spheroid of tissue (**B**) and develops into a mucociliary epithelium, becoming motile after 3-4 days of culture at 14°C (**B′**). The second method dissociates the animal cap material in calcium free, magnesium free media, and the pigmented superficial ectoderm is discarded (**C**). The dissociated cells are then transferred to 0.75x MMR and mechanically pushed into a pile, which naturally adheres (**D**). The aggregates forms into a spheroid of tissue (**D′**) which becomes motile after 3-4 days of culture at 14°C. Various morphologies can be given to parent organisms via surgical forceps and a microcautery electrode (**E**), allowing for the production of semi-toroidal shapes [shown in **F**, next to a spheroid (white arrow head in F) and shaped from reaggregated cells in **F′**], moderately compressed spheroids (**G,** lateral view **G′**), and toroids (**H**). Scale bars indicate 500 microns.

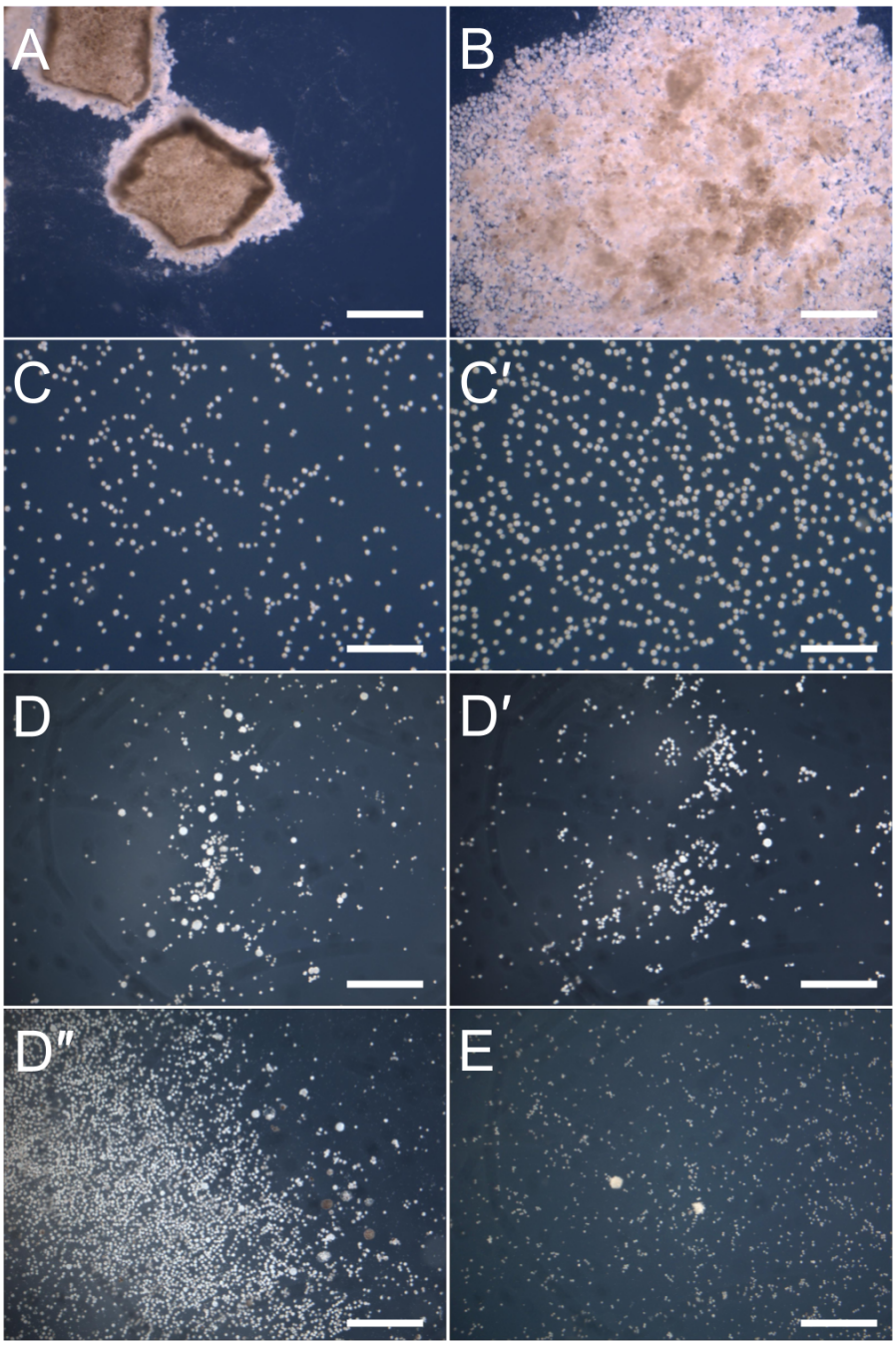

Fig. S2. Reconfigurable organisms are required for the generation of offspring. Dissociated stem cell layers are produced from animal cap tissue of Nieuwkoop and Faber stage 9 embryos (**A**), which naturally dissociates when placed in calcium-free, magnesium-free media (**B**). Pooled and washed cells can then be deposited into dishes at various concentrations (**C**, **C′**), providing the necessary material for self replication. This process required reconfigurable organisms to be present: offspring were never produced across three trials with dissociated stem cells only (**D**-**D″**). Any small aggregates fall apart over proceeding days of development, and no motile offspring were observed after 5 days (**E**). Scale bars indicate 500 microns.

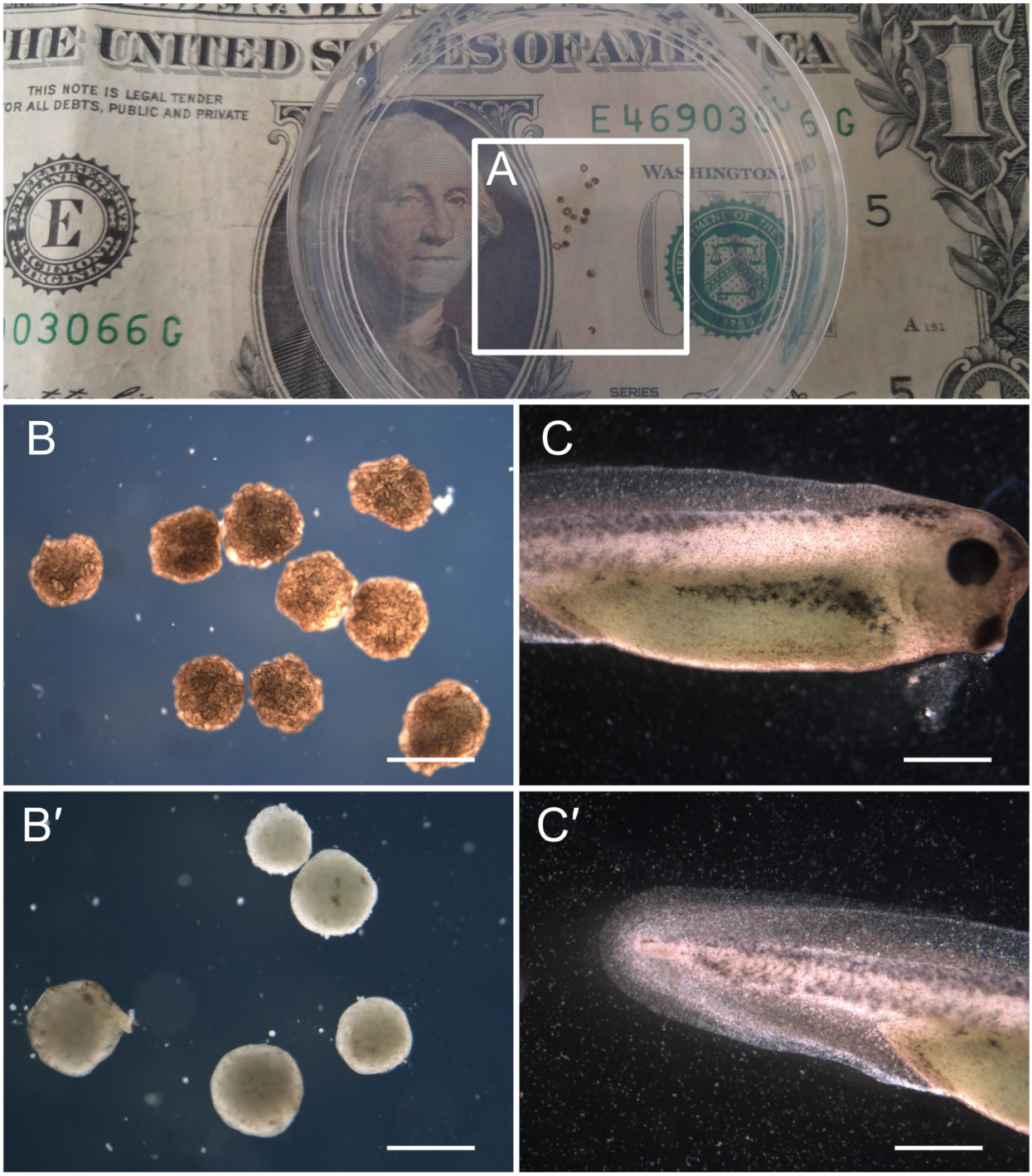

Fig. S3. Relative size of the self-replicating organisms. (**A**) It can be difficult to conceptualize 500 microns, so C- and O shaped designs were placed on top of a US dollar bill for comparison. Wild type reconfigurable organisms healed from an animal cap (**B**), and reconfigurable organisms formed by manually dissociating and reassociating the stem cells contained within a cap (**B′**), are shown at the same magnification beside a tadpole (**C**,**C′**), also at the same magnification: Scale bars indicate 500 microns.

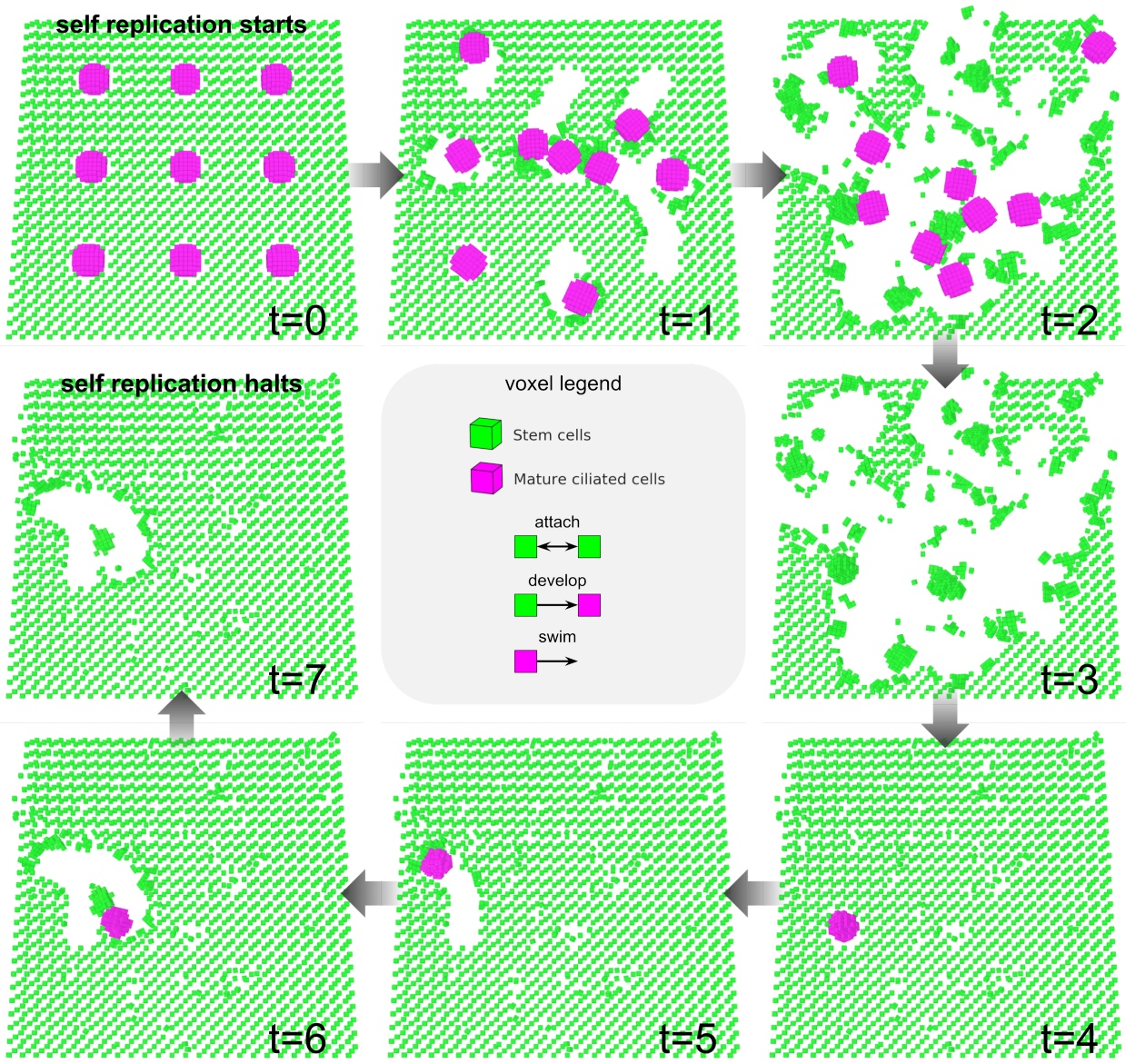

Fig. S4. Modeling kinematic self replication. [*Clockwise from top left*:] A swarm of nine virtual wild type spheroids (parents; pink) are placed in a virtual petri dish that is lined with virtual dissociated stem cells (green). As the swarm moves through the dissociated stem cells, piles of stem cells are formed (t=2). The parents are then removed (t=3), and any piles larger than a preselected threshold, develop from piles to motile offspring (green to pink) (t=4). More dissociated cells are injected into empty space in the dish, and pile building restarts. Here, a single filial generation was produced, then replication stopped (t=7). On average, simulated wild type spheroids did not produce piles larger than the selected threshold of two thirds the size of a wild type spheroid. This threshold was set higher than the biological data suggested: piles approximately one fifth the diameter of the initial parents could develop into motile offspring. However, small children are likely to produce even smaller grandchildren, or none at all. Because each filial generation is computationally expensive, we increased the threshold to create a more conservative filter: only the settings that result in the largest offspring and the most replication will pass through the filter and be allotted computational resources.

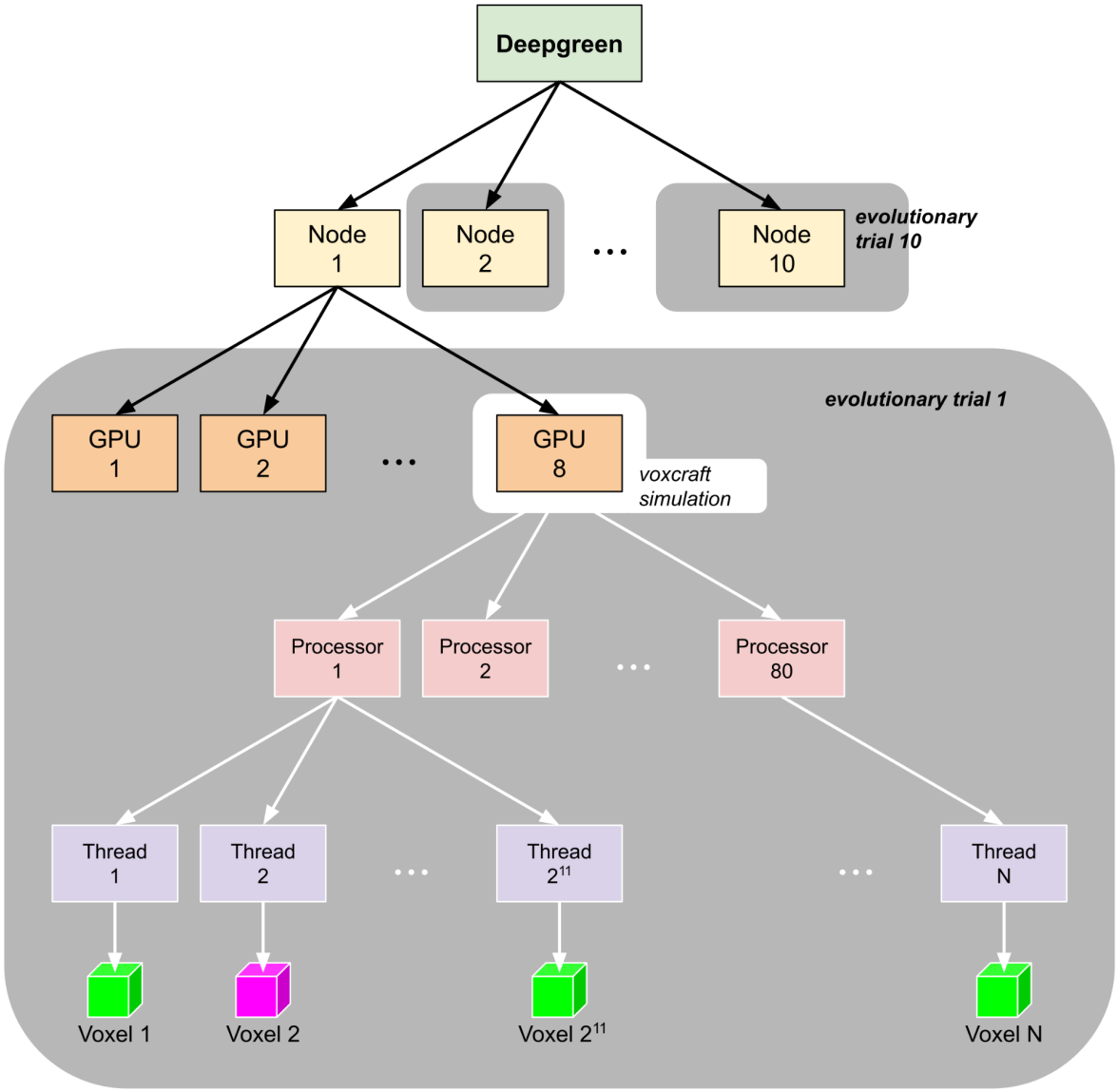

Fig. S5. GPU-accelerated simulations. Deepgreen is a high performance computing cluster at the University of Vermont which contains ten Nvidia GPU nodes. Each Nvidia node has eight Tesla V100s that are capable of running the CUDA programming platform, which was a requirement of the employed simulator, voxcraft-sim. We parallelized evolutionary trials across different nodes: On each node, an independent trial maintained a population of 16 designs, which were evaluated in batches of eight designs at a time, in parallel, across the node's eight GPUs. Each simulation contains a single design, which consists of N voxels. At each time step of simulation (numerical integration), the dynamics (position, velocity and acceleration) of each voxel within a simulation (on the order of 10^4 to 10^5 voxels) were evaluated concurrently on separate threads. Note that the number of voxels that can be updated in parallel will be constrained by the main memory bandwidth well before the number of voxels approaches the total number of potentially independent threads ($80 \times 2^{11} = 163{,}840$).

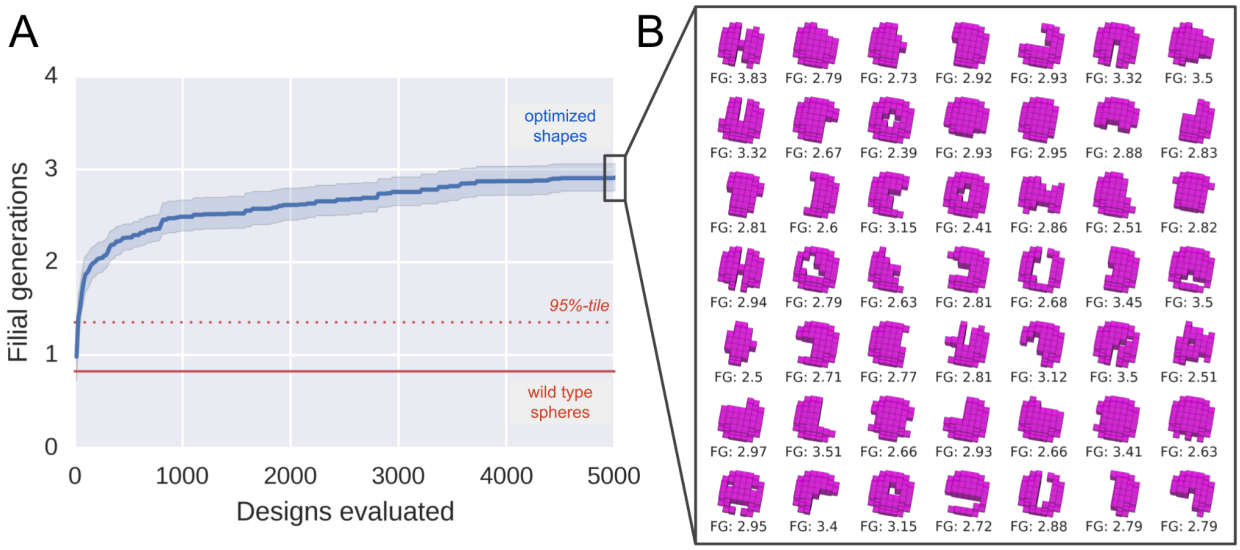

Fig. S6. Amplifying self replication via morphology optimization *in silico*. Forty nine optimization trials were conducted (**A**), each of which starts with the evaluation of a swarm of wild type spheroids, *in silico*, under random swimming trajectories as derived from a unique set of random cilia forces. These 49 independent random cilia forces were held constant while body shape was optimized. Starting from 49 different randomly generated populations of 16 body shapes, the optimizer randomly removes voxels from the sphere, selecting shapes that result in more self replication. At the end of optimization, the highest amount of self replication produced by each of the 49 trials (**B**) was compared against the amount of self replication produced by the wild type spheres. The solid blue and red lines indicate mean fitness (whose integer part is the number of filial generations produced; Eqn. 1) across optimization time *in silico* for the optimized and wild type body shapes, respectively. Ninety-five percent bootstrapped confidence intervals (95%- and 5%-tiles) are drawn as shaded blue regions around the mean fitness of the optimized design; the dotted red line denotes the 95%-tile of fitness for the wild type spheres.

Fig. S7. Controlling self replication via terrain optimization *in silico*. There are many tunable parameters that affect the efficacy of kinematic self replication in reconfigurable organisms. In addition to optimizing organism shape to increase self replication, we optimized the structure of the terrain. Black, immovable and unpassable voxels were added along the surface of each simulated petri dish. These barriers act as guide rails, channeling the random swimming of the unsculpted wild type spheres (pink) along certain trajectories. Instead of determining where to carve away tissue from a spherical body, the optimization algorithm now determines where to place black voxels on the surface plane. Random terrains trap the organisms, inhibiting self replication (*top row*). Optimized terrains reliably increased self replication compared to both random terrains and flat terrains without black voxels.

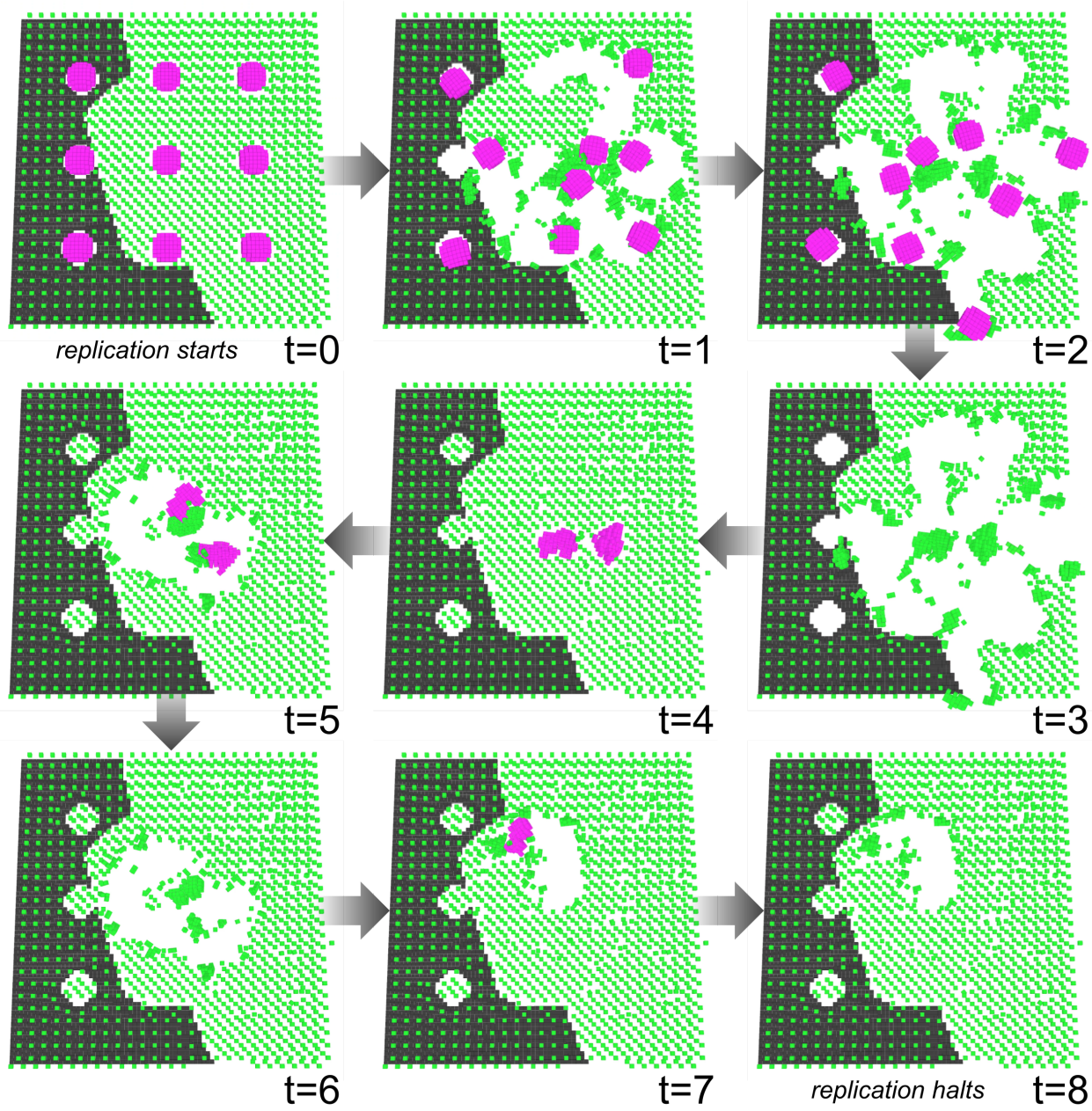

Fig. S8. An optimized terrain that amplifies self replication in wild type reconfigurable organisms. One of the optimized terrains (black voxels) that amplified self replication *in silico*, yielded two filial generations of pile building after the initial swarm. On flat terrain (without black voxels), no replication occurs on average: the average number of filial generations is below one.

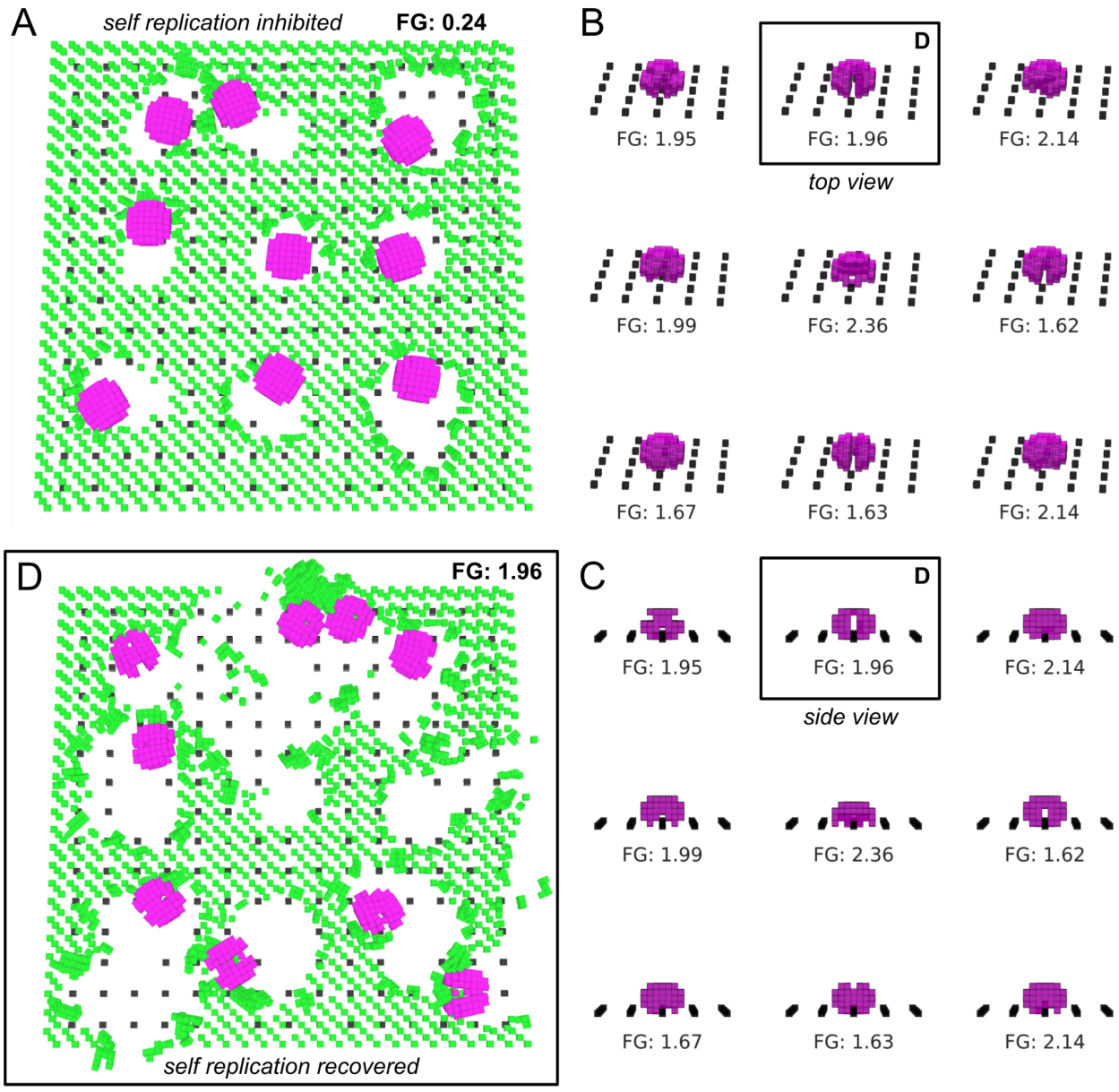

Fig. S9. Recovering self-replication in a cluttered environment *in silico*. A static grid of unpassable black voxels were placed on the bottom of the simulated dish. In this cluttered environment, the wild type spherical organisms could no longer move enough to build offspring (**A**). Their ability to spontaneously self-replicate was lost. However, by optimizing organism shape, self replication can be recovered. The results of nine independent evolutionary trials are shown here at two different perspectives: from above (**B**) and from the side (**C**). The evolutionary algorithm discovered how to raise the organisms on stilts so they can glide over the top of the clutter and rescue function: aggregating loose stem cells into piles large enough to develop into offspring (**D**).

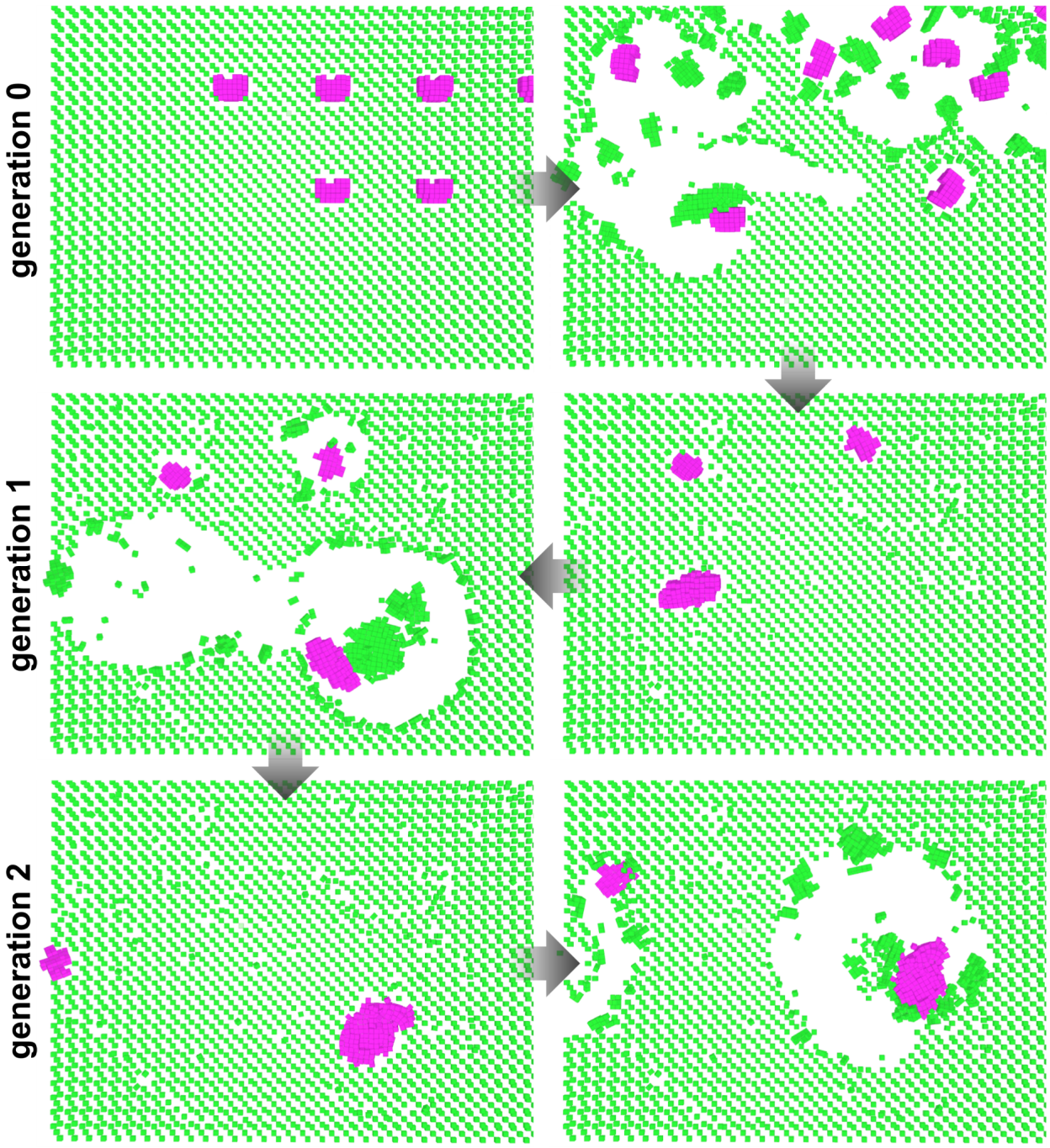

Fig. S10. Increasingly larger offspring *in silico*. Reconfigurable organisms can create offspring that are larger than parents, and this enlarging process can persist for multiple rounds of replication *in silico*.

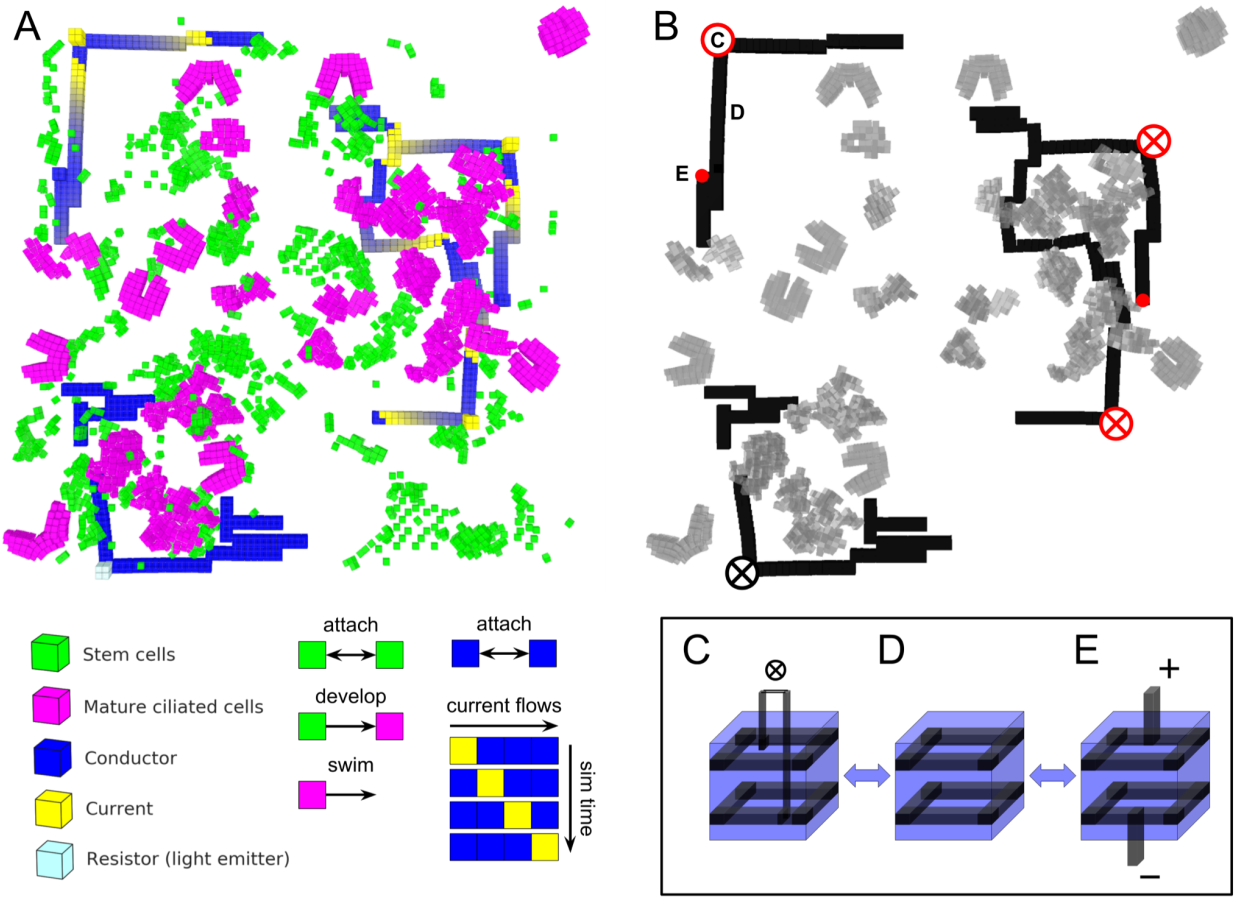

Fig. S11. The simulated circuit completion task. A swarm of simulated kinematically self-replicating reconfigurable organisms was placed inside a petri dish alongside simulated modular electronic components (**A**) that can freely move and rotate along a surface plane, and connect on contact. For clarity, the dish is shown in grayscale, without the loose stem cells (**B**). There are three simulated electronic modules: light emitter (**C**), wire (**D**), and power supplies (**E**).

Table S1. The parameters of kinematic self replication in reconfigurable organisms. Properties of the environment (blue; 1-5), reconfigurable organisms (red; 6-16), and dissociated stem cells (green; 17-26) are grouped under these three categories, enumerated and color coded.

no.	Parameter	In vivo	In silico
1	Temperature	18-20°C	N/A
2	Size of dish	60mm in diameter	Soft 81×81×5 boundaries.
3	Arena substrate	1% agarose dissolved in 0.75x MMR	Coulomb friction: 1.0 and 3.0 static and dynamic coefficients, respectively.
4	Terrain characteristics	Solidified gelatin	Surface plane
5	Wall forces	The substrate forms a gradual incline at the edge of the dish, due to the meniscus formed during agarose cooling. Reconfigurable organisms were rarely seen at the very edge.	A soft constraint that gradually pushes organisms back toward the center of the dish, if they move outside predefined bounds.
6	Initial parents' starting position	Deposited in center of dissociated stem cells from above	Evenly spaced in a 3 by 3 grid, 15 voxel lengths apart, in the center of the dissociated stem cells.
7	Number of initial parents	12	9 during optimization: just enough to observe self replication occur while keeping the total number of voxels below 3000 to reduce simulation time.
8	Number of cells in parents	~3,000	161 voxels
9	Volume of initial parents	0.065-0.130 cubic mm	161 voxel length^3
10	Length of initial parents.	400-600µm	7 voxels wide
11	Shape of initial parents	spheroids, toroids, semi-toroid, compressed	see Fig. S6

12	Width/height of initial parents	spheres: 1:1, toroids and semitoriods: 3:1, compressed 4:1	7:5 voxel aspect ratio
13	Cilia force	PIV analysis	Impulse forces mediated by global damping.
14	Collisions	Cells and tissues deform elastically.	Voxels are elastic: they deform against objects and recoil from them.
15	Replication time length	20 hours	3.5 seconds (16,366 time steps, step size 0.000214 sec)
16	Time to senescence	10 days	3 seconds of simulation time, which was sufficient for simulated spheroids to collide with about as many dissociated cells as physical spheroid progenitors, given a density of 50 cell/mm^2 (Fig. 2*E*). This was done by visual inspection of the physical and simulated spheroids. Simulation time could be more accurately estimated by computing the mean time it takes for simulated spheroid progenitors to collide with exactly the number of dissociated cells encountered by the physical spheroid progenitors.
17	Type of dissociated stem cell	*Xenopus laevis* species embryonic cells (stage 10)	Adhesive voxel singletons.
18	number of dissociated cells	~60,000	1000-2000 voxels
19	Density of dissociated stem cells	25-150 cells/mm2	0.15-0.30 voxels / u^2, where u = length of one unstretched voxel.
20	Distribution of dissociated stem cells	Random distribution without any aggregate clumps.	Uniform distribution within a 81×81×3 bounding volume, without any initially touching

			each other or the organisms.
21	Area covered by dissociated stem cells	No data	81×81 voxel lengths
22	Stem cell stickiness	Contact adherence	Collision radius of 0.85 voxel lengths.
23	Stem cell spherification	Adhesion properties lead to a minimized surface area to volume ratio.	Stochastic detachment of chains of voxels within a pile of stem cells; pile force pulling stochastically detached cells inward.
24	Size of pile that develops into stable offspring that maintain adherence ~4d but are not self motile.	Minimum size = 50 cells, ~1.7% of default adult size (50/3000)	When optimizing body shape, a threshold of 108 voxels, 66% the size of default simulated spheroids (161 voxels). Higher threshold set to compensate for other, unknown simulation inaccuracies. When forecasting utility, a threshold of 40 voxels, 25% the size of default simulated spheroids. Forty voxels is the best estimate for the minimum size of piles that developed into self motile offspring in vivo.
25	Size of pile that develops into stable and mobile offspring that are able to self replicate for 10-14d.	One fourth the default adult diameter.	Two-thirds and one-fourth for shape optimization and utility forecasting, respectively.
26	Development time from pile to adult	4 days	0.5 seconds of simulation time.

Supplemental Data S1.

The sizes of the largest first generation offspring, and the total number of generations of self replication produced, is recorded for eight independent trials here:

Shape	sphere	sphere	sphere	C shape	2x size sphere	flattened sphere	C shape	C shape	noparent	noparent	noparent
Cell Density (cells/mm2)	25	75	150	61	52	105	61	91	61	83	150
1	0.150529	0.3148237	0.462979	0.4521711	0.2709368	0.5708763	0.4383921	0.6386021	0.075905263	0.073165789	0.078242105
2	0.150529	0.3090947	0.3746105	0.4222342	0.2563316	0.2848421	0.3548237	0.4772063	0.071828947	0.071102632	0.074105263
3	0.1445211	0.2879395	0.3114158	0.3721605	0.2349632	0.2837237	0.3314105	0.4711292	0.071052632	0.063268421	0.072260526
4	0.1271895	0.2832842	0.3016579	0.3390132	0.2306789	0.2662974	0.3000474	0.4204208	0.066418421	0.059136842	0.069526316
5	0.1227579	0.2292947	0.2966579	0.3316211	0.2193553	0.253071	0.2992605	0.41675	0.064513158	0.057894737	0.067247368
6	0.1159079	0.2160474	0.2848421	0.31915	0.1972816	0.2336026	0.2852816	0.3883958	0.064084211	0.053673684	0.066989474
7	0.1118974	0.2085421	0.2834289	0.3051737	0.1907842	0.2221158	0.2686263	0.3793729	0.063157895	0.052697368	0.065789474
8	0.1106526	0.1935237	0.27555	0.294971	0.1854105	0.2183421	0.26635	0.3611813	0.061434211	0.049652632	0.059663158
9	0.1059184	0.1671842	0.253179	0.2779026	0.1842105	0.2158526	0.2570342	0.3286396	0.061434211	0.047442105	0.058431579
10	0.1005526	0.1652658	0.2522474	0.2717026	0.1824737	0.2106579	0.2542158	0.323275	0.061378947	0.047442105	0.058431579
average	0.12404554	0.2375	0.30965685	0.33861	0.21524263	0.27593815	0.30554421	0.4204973	0.066120789	0.057547632	0.067068684
stdev	0.018580811 88	0.05696704 612	0.06404447 675	0.06020963 588	0.03211403 749	0.10730149 19	0.05687541 276	0.09279210 633	0.005106147	0.009238478	0.006774704
generations produced	**1**	**1**	**2**	**3**	**1**	**1**	**2**	**4**	**0**	**0**	**0**
							contamination				